Journal of Magnetic Resonance 212 (2011) 216–223

Contents lists available at ScienceDirect

Journal of Magnetic Resonance

journal homepage: www.elsevier.com/locate/jmr

NMR velocimetry with 13-interval stimulated echo multi-slice imaging in natural porous media under low flow rates

Natascha Spindler [a], Petrik Galvosas [b,*], Andreas Pohlmeier [a], Harry Vereecken [a]

[a] Forschungszentrum Juelich, Institute of Bio- and Geosciences – Agrosphere, 52425 Juelich, Germany
[b] MacDiarmid Institute for Advanced Materials and Nanotechnology, School of Chemical and Physical Sciences, Victoria University of Wellington, Wellington 6001, New Zealand

ARTICLE INFO

Article history:
Received 9 March 2011
Revised 30 June 2011
Available online 12 July 2011

Keywords:
NMR flow mapping
Natural porous media
Internal magnetic field gradients

ABSTRACT

Characterization and quantification of root water uptake processes play a key role in understanding and managing the effects of global climate change on agricultural production and ecosystem dynamics. Part of this understanding is related to the flow of water towards plant roots in soils. In this study we demonstrate for the first time, to our knowledge, that fluid flow in the voids of the pore space of a model soil system (natural sand) can be detected and mapped to an NMR image for mean flows as low as 0.06 mm/s even under the influence of internal magnetic field gradients. To accomplish this we combined multi-slice imaging with a 13-interval pulse sequence to the NMR pulse sequence 13-interval stimulated echo multi-slice imaging (13-interval STEMSI). The result is a largely reduced influence of the internal magnetic field gradients, leading to an improved signal-to-noise ratio which in turn enables one to acquire velocity maps where conventional stimulated echo methods fail.

1. Introduction

Understanding root water uptake in soils is of high importance for securing nutrition in the context of climate change and linked phenomena such as strongly varying weather conditions (drought, heavy rain). One step to understand how root water uptake occurs is the knowledge of water flow in soil towards plant roots – the "hidden half" of plants [1].

Processes in the rhizosphere have previously been experimentally investigated with non-NMR methods either invasively or in restricted geometries such as 2D rhizotrones [2]. Transport processes in soil were investigated with experimental black-box methods combined with model calculations to characterize the internal structure of porous media. Invasive probes such as time domain reflectometry (TDR) [3] or in situ extraction of the liquid phase [4] yield information about empirical parameters such as water content and solute composition at a few defined sites inside the sample. Although these methods may determine the heterogeneity of the sample in a parametrized way, they return no information at the actual spatial structure on the length scale of the pore size or smaller.

Magnetic resonance techniques are capable of providing a more detailed picture of the root–soil system and have therefore received significant attention as a method for the non-invasive investigation of plants and soil. With magnetic resonance imaging (MRI) three-dimensional (3D) structures in plants [5,6], root systems, as well as indirect water uptake [7–11] have been studied. Theoretical concepts have been published recently [12–14], which provide a sound base for comparison with experimental studies for deeper understanding of the uptake mechanism. This now needs to be matched by a broader experimental knowledge of the hydraulic properties of the fluids in the porous medium by measuring water flow dynamics through the soil pore space and the root system.

Although MRI offers direct observation of fluxes by flow imaging techniques [15], it has been used mainly for investigations of flow rates ranging from 1 m/s [16,17] down to several mm/s [18]. Even lower flow rates for water in plants and wheat grains have been reported by Scheenen et al. [19] and Jenner et al. [20], respectively. Recently van de Meent et al. [21] obtained velocity maps in algae for averaged flow rates of about 45 μm/s at observation times of 500 ms. While this is in the range of water flux in soil caused by uptake from roots (for instance flow rates in bean root xylem vessels are reported by Schulze-Till et al. [22] between 340 μm/s and 770 μm/s), here we face the additional and severe challenge of the heterogeneity of the soil structure and the NMR artifacts linked to it. Therefore, water uptake in roots and the surrounding soil has been monitored only indirectly with tracer substances [23] by NMR so far.

Measuring local velocities in porous media by combining flow encoding with imaging techniques is widely used and can be found in numerous publications [such as 24–32]. Among other influences, Homan et al. [32] investigated the effects of internal

* Corresponding author. Fax: +64 4 463 5237.
E-mail address: petrik.galvosas@vuw.ac.nz (P. Galvosas).

1090-7807/$ - see front matter © 2011 Elsevier Inc. All rights reserved.
doi:10.1016/j.jmr.2011.07.004

magnetic field gradients on NMR flow measurements. They consistently found an increasing impact of internal magnetic field gradients (as well as relaxation) on both the signal magnitude and the obtained velocities with increasing observation time. To address this issue, one can combine the approach of Cotts et al. [33] for the reduction of the influence of internal magnetic field gradients with appropriate imaging techniques as carried out by Li et al. [31] for flow mapping or by Lucas et al. [34] for diffusion mapping. Li et al. [31] used SPRITE for the imaging component of the pulse sequence. Following the same approach Romanenko et al. [35] was able to improve the spatial resolution substantially.

In this work we use interleaved multi-slice imaging instead of SPRITE as an alternative way of mapping flow in porous media. We present flow mapping in the pore space of natural sand as a model system for soil, covering velocities typical for water uptake in the vicinity of plant roots and in the roots themselves. In order to reduce the influence of internal magnetic field gradients on the MRI signal, interleaved multi-slice imaging was combined with the 13-interval pulsed field gradients (PFG) stimulated echo pulse sequence as introduced by Cotts et al. [33] for flow encoding. We strictly adhere to the condition which requires the centering of the flow encoding gradients between rf-pulses (see [33] for details) in order to achieve the maximum suppression of the internal magnetic field gradient's influence. Since this is often linked to a signal loss due to enhanced T_2 relaxation we partially compensate for this loss by merging the imaging elements of the experiment into the scheme of the 13-interval sequence. We call this new pulse sequence 13-interval STEMSI according to 13-interval stimulated echo multi-slice imaging.

One possible application of the 13-interval STEMSI (if performed with contiguous slices) could be the acquisition of 3D flow paths (as typical for angiography) which may aid the correction of MRI artifacts. Therefore, in this work, we aim for a resolution which roughly matches the diameter of the roots as well as the pores in the soil system. A resolution in the order of 0.1 mm appears to be sufficient to determine averaged velocities within the root (or the pore), and allow tracking of the flow in the heterogeneous 3D structure. A resolution beyond the root diameter or pore sizes is unnecessary in this context.

2. Theory

The attenuation of an NMR echo can be described according to Callaghan [15] using

$$M(t_e) = M_0(t_e) \times \Psi(t_e) \times \psi(t_e) \text{ with} \tag{1}$$

$$\Psi(t_e) = \exp\left\{-D\gamma^2 \int_0^{t_e} dt' \left[\int_0^{t'} dt'' \boldsymbol{G}^*_{tot}(t'')\right]^2\right\}, \tag{1a}$$

$$\psi(t_e) = \exp\left\{i\gamma \boldsymbol{v} \int_0^{t_e} dt' \int_0^{t'} dt'' \boldsymbol{G}^*_{tot}(t'')\right\}, \tag{1b}$$

$$\text{whereby } \boldsymbol{G}^*_{tot}(t) = \boldsymbol{G}^*(t) + \boldsymbol{g}^*(t). \tag{1c}$$

$M(t_e)$ is the amplitude at the echo time t_e, which can be expressed by the signal intensity $M_0(t_e)$ without external applied magnetic field gradients ($\boldsymbol{G}(t) = 0$), influenced by molecular diffusion $\Psi(t_e)$ and a phase factor $\psi(t_e)$ due to the velocity contribution. T_1 and T_2 relaxation effects are already included in $M_0(t_e)$. γ is the gyromagnetic ratio, D is the diffusion coefficient, $\boldsymbol{v}$ the velocity of the molecules, and $\boldsymbol{G}^*_{tot}(t)$ denotes the sum of all effective applied ($\boldsymbol{G}^*(t)$) and internal ($\boldsymbol{g}^*(t)$) magnetic field gradients (for the concept of effective magnetic field gradients see [36]).

According to Galvosas et al. [37], the integral in Eq. (1a), expressing the contribution of diffusive processes, can be rewritten by inserting Eq. (1c) into Eq. (1a) as

$$\int_0^{t_e} dt' \left[\int_0^{t'} dt'' \boldsymbol{G}^*_{tot}(t'')\right]^2 = A_p(t_e) + A_c(t_e) + A_b(t_e) \text{ with} \tag{2}$$

$$A_p(t_e) = \int_0^{t_e} dt' \left[\int_0^{t'} dt'' \boldsymbol{G}^*(t'')\right]^2, \tag{2a}$$

$$A_c(t_e) = 2\int_0^{t_e} dt' \int_0^{t'} dt'' \boldsymbol{G}^*(t'') \int_0^{t'} dt'' \boldsymbol{g}^*(t''), \tag{2b}$$

$$A_b(t_e) = \int_0^{t_e} dt' \left[\int_0^{t'} dt'' \boldsymbol{g}^*(t'')\right]^2. \tag{2c}$$

Here, $A_p(t_e)$, $A_c(t_e)$ and $A_b(t_e)$ are separate terms influencing the NMR signal amplitude, caused by: the applied pulsed field gradients alone; the so called cross term between the applied and the internal magnetic field gradients; and the internal gradients alone, respectively.

However, considering the term in Eq. (1) responsible for the imparted phase factor due to flow as expressed by Eq. (1b), one may easily find that there is no contribution from a cross term. This can be seen by inserting Eq. (1c) into Eq. (1b),

$$\int_0^{t_e} dt' \int_0^{t'} dt'' \boldsymbol{G}^*_{tot}(t'') = \boldsymbol{B}_p(t_e) + \boldsymbol{B}_b(t_e) \quad \text{with} \tag{3}$$

$$\boldsymbol{B}_p(t_e) = \int_0^{t_e} dt' \int_0^{t'} dt'' \boldsymbol{G}^*(t''), \tag{3a}$$

$$\boldsymbol{B}_b(t_e) = \int_0^{t_e} dt' \int_0^{t'} dt'' \boldsymbol{g}^*(t''), \tag{3b}$$

where $\boldsymbol{B}_p(t_e)$ and $\boldsymbol{B}_b(t_e)$ describe the influence on the NMR signal with respect to the applied pulsed field gradients and the internal gradients under flow, respectively. Evidently, there is no influence on the imparted phase factor ψ arising from a cross term. However, the signal amplitude M may be influenced significantly via Ψ by the diffusion cross term, A_c, and the internal field gradient term itself, A_b. This may render the application of standard NMR diffusometry pulse sequences (such as proposed by Tanner [38]) impossible, due to an insufficient signal-to-noise ratio. The 13-interval pulse sequence with bipolar pulsed field gradients as proposed by Cotts et al. [33] is suited to reducing the influence of exactly those two terms, A_c and A_b, thus recovering the detected NMR signal. We therefore combined the 13-interval pulse gradient scheme for flow encoding with MR imaging for the detection of spatially resolved velocity maps.

3. Materials and methods

The pulse sequence used in this work is a combination of interleaved multi-slice imaging (black gradient pulses in Fig. 1) with a 13-interval sequence (gray gradient pulses in Fig. 1), which we name the '13-interval stimulated echo multi-slice imaging' pulse sequence (13-interval STEMSI). This pulse sequence contains two pairs of bipolar pulsed field gradients, separated by the observation time Δ. Each pulsed field gradient (with the intensity $G = |\boldsymbol{G}|$ and width δ) is symmetrically centered in the τ intervals in order to minimize the influence of internal magnetic field gradients [33]. During the storage interval (Δ') the magnetization is stored along the direction of the external polarizing magnetic field $\boldsymbol{B}_0$ (z-direction), so as to be only influenced by T_1 relaxation. On the other hand, internal magnetic field gradients $\boldsymbol{g}(t)$ and T_2 relaxation can

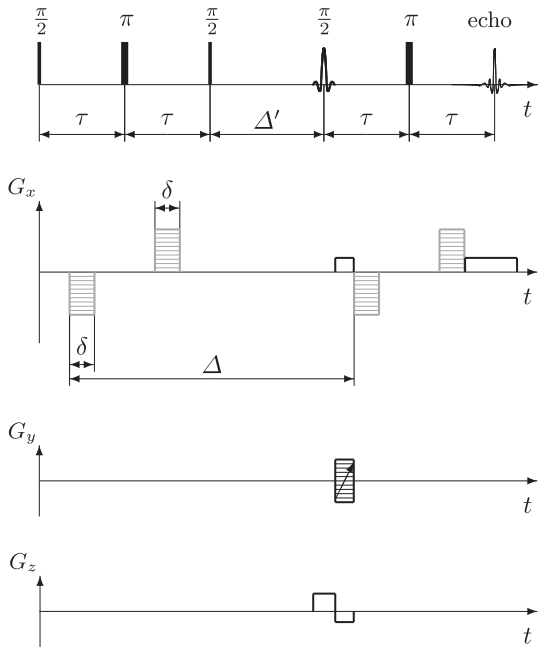

Fig. 1. Combined 13-interval pulse sequence with multi-slice imaging, 13-interval STEMSI. Note that the pulsed field gradients (gray) can also be applied in *y*- or *z*-direction.

only affect the NMR signal during the τ intervals. Note that the pulsed field gradients (gray) can also be applied in *y*- or *z*-direction.

Flow encoding measurements are based on the detection of the phase shift $\Delta\phi(t_e)$ of the NMR signal (see [15] for details). It is easy to see that this phase shift can be derived from the expression in the exponent of Eq. (1b) by evaluating the containing integral as given by Eq. (3). For the further analysis of this equation we will assume (similar to Galvosas *et al.* [37]) that internal gradients, as experienced by the diffusing molecules, may change during the storage interval Δ', but stay constant before and after Δ' with values of $\boldsymbol{g}$ and $\boldsymbol{f}$, respectively. Since $\boldsymbol{G}(t)$ is explicitly known (see the gray pulsed field gradients for phase encoding in Fig. 1), we obtain

$$\psi(t_e) = \exp\{i\gamma \boldsymbol{v}[2\delta\Delta\boldsymbol{G} + \tau^2(\boldsymbol{g} - \boldsymbol{f})]\}. \quad (4)$$

Eq. (4) highlights another advantage of the 13-interval simulated echo over the standard stimulated echo. Not only does it reduce the impact of the internal gradients on the NMR signal amplitude, Ψ (as discussed earlier), it also reduces their impact on the imparted phase factor ψ. In the special case of constant internal gradients their influence is fully compensated, which is impossible to achieve with the standard stimulated echo [38], as a term $\Delta\tau\boldsymbol{g}$ always survives. Even in the case $\boldsymbol{g} \neq \boldsymbol{f}$, we may neglect the impact of internal field gradients, since $\tau^2 \ll 2\delta\Delta$ and $(\boldsymbol{g} - \boldsymbol{f}) \ll \boldsymbol{G}$ will be satisfied in most cases. However, we may remove the influence of the internal field gradients entirely by dividing each measurement conducted with pulsed field gradients by the measurement without pulsed field gradients, thus subtracting the term due to the internal gradients in the exponent of Eq. (4). The remaining expression yields a phase change of the NMR signal independent of the internal field gradients, with

$$\Delta\phi(t_e, \boldsymbol{r}) = 2\delta\Delta\gamma\boldsymbol{G}\boldsymbol{v}(\boldsymbol{r}). \quad (5)$$

This relation already takes into account that the velocity is a local property and we expect to obtain phase differences depending on the position in the sample. Moreover, velocities in one voxel are likely to be distributions, leading to a distribution of phase differences. We accounted for that by obtaining the averaged velocity in each voxel using the small gradient pulse approximation [39,40] in combination with Eq. (5).

All NMR experiments were performed on a wide-bore Bruker AVANCE 400, which was equipped with a 3D microimaging system Micro2.5 (Bruker). It provided a maximum gradient strength of 1.45 T/m and a 15 mm inner diameter birdcage resonator with an RF sensitive height of 20 mm. The acquired NMR data were processed with Prospa® (Magritek Ltd., Wellington, New Zealand). Any fitting procedures were done subsequently with Origin® (OriginLab Corporation, Northampton, MA, USA).

The main component of the experimental setup for flow imaging was a polyvinyl chloride column with an inner diameter of d_i = 13.5 mm and a length of 95 mm. This column was filled with natural sand (FH 31, Quarzwerke Frechen GmbH, Frechen, Germany; components: 99.7% SiO_2, 0.1% Al_2O_3, and 0.04% Fe_2O_3), which is characterized by a mean grain size of about d_g = 0.35 mm, an averaged pore diameter between the grains of about 0.1 mm and a specific surface area of 71 $cm^2\,g^{-1}$. The porosity $\theta = 0.35 \pm 0.01$ was determined by the water content of the fully water saturated sand column. This sand is a reference system in the "Institute of Bio- and Geosciences – Agrosphere" and is chosen for its high hydraulic conductivity as well as its relatively low iron oxide content.

Water doped by 0.1 wt% $CuSO_4$ was pumped through the sand column using a peristaltic pump with variable volume flow. Thus, we applied a water flow in the *z*-direction, which is parallel to the static magnetic field [41]. To determine the applied pore flow velocities, v_{app}, we measured gravimetrically the volume flow, J_{app}, at each chosen pump flow rate. From these volume flows we calculated the pore flow velocities by taking into account the cross-sectional area $A = \pi(d_i/2)^2$ of the sand column and the porosity, θ, according to $v_{app} = J_{app}/(\theta A)$. The applied pore flow velocities ranged from a maximum of $v_{app,max}$ = 1.35 mm/s down to a minimum of $v_{app,0}$ = 0.02 mm/s. To ensure a homogeneous flow field all over the sample, a reservoir of 0.1 wt% $CuSO_4$-doped water was included in the setup and filled to a higher level than the top of the sample tube inside the NMR magnet. This led to a completely water saturated sand column. To ensure continuous water flow through the sand column, regardless of any unsteadiness caused by the peristaltic pump, a second reservoir was included in the experimental setup right after the pump (see [41] for details). In order to avoid rearranging or repacking of the sand inside the column, the experiments were started at high pore flow velocities and then reduced stepwise to lower pore flow velocities until the flow detection minimum was reached.

Flow encoded MRI acquisition was performed with a field of view of $18.0 \times 18.0 \times 4.0\ mm^3$ and a matrix size of $128 \times 128 \times 4$. This would result in a spatial resolution of 0.14 mm/pixel with a slice thickness of 1 mm for a homogeneous sample. However, due to the heterogeneity of the magnetic susceptibility in the sand we have a $T_2^* \approx 0.35$ ms, resulting in a line width (at full width half maximum) of about 900 Hz. To account for this line broadening all time domain data where acquired with the highest available spectral width of 100 kHz. Even under these conditions one pixel may be smeared out by half a pixel into its neighbors, thus reducing the effective resolution.

The 3D data sets are composed of the desired number of slices situated next to each other with zero gap. The slices are sampled interleaved, ordered by odd and even numbers. Imaging was orientated perpendicular to the axis of the sand column to get cross-sectional velocity maps. Thus, the slice selection gradient of 0.261 T/m was applied in *z*-direction while a sinc-shaped soft pulse (truncated after the third zero) of 0.5 ms irradiated the sample. Phase gradients (0.05 T/m, length 1.69 ms) and read gradients (0.13 T/m) were applied in the *xy*-plane. The repetition time was

TR = 2.0 s over which the acquisition of individual slices was distributed equally (four slices for the current experiments). The $\pi/2$ pulses had a length of 19 μs while the T_2 sensitive time, τ, between the $\pi/2$ and π pulses was set to 2.3 ms. To achieve a sufficient signal-to-noise ratio, 32 scans per gradient step were performed and linked to a 32 step phase cycle (a full phase cycle for the Hahn echo subsequence after the storage time Δ' extended by an add-subtract scheme for the suppression of unwanted signals from spins already relaxed back at the time of the soft rf-pulse). Shorter phase cycle schemes are possible.

The flow encoding was done utilizing two gradient values $\boldsymbol{G}$. The gradient pulse duration was $\delta = 0.3$ ms, with a maximum gradient strength of up to $G = 0.345$ T/m and $G = 0.921$ T/m for detecting the highest and lowest applied flow velocities, respectively. Flow-encoding gradients were applied both parallel (in the z-direction) and perpendicular (in the x- and y-directions) to the applied water flow. For flow mapping, the observation time was held constant at $\Delta = 17.0$ ms. However, for investigating the dependence of the MRI-detected mean pore flow velocity on the observation time, Δ was varied in the range from $\Delta_{min} = 9$ ms up to $\Delta_{max} = 50$ ms at a fixed flow of $v = 1.35$ mm/s. The measurement time for one velocity map was 3.5 h (this includes the 32 scans, 128 increments for the imaging phase gradient and two values of the flow encoding gradients). After each experiment, in which the applied flow velocity was decreased, no NMR experiments were conducted until 24 h later, to ensure the lower water flow is in equilibrium.

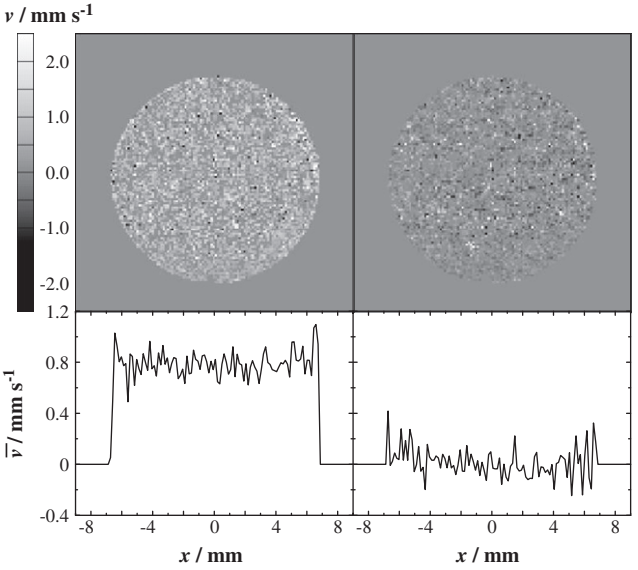

Fig. 2. Velocity maps (top) and 1D mean velocity profiles (bottom) of the highest applied pore velocity of $v_{app,max} = 1.35$ mm/s using the pulse sequence 13-interval STEMSI. Shown are the results of flow encoding parallel (z-direction, left) and perpendicular (x-direction, right) to the induced water flow direction. The observation time is 17 ms.

4. Results and discussion

Initial attempts to acquire velocity maps with a standard unipolar pulse sequence [38] were unsuccessful. Even at observation times as short as $\Delta = 10$ ms, the acquired images contained mainly noise, which made the usage of the 13-interval pulse sequence indispensable. Therefore, flow-encoded MR images were recorded at the highest applied pore flow velocity of $v_{app,max} = 1.35$ mm/s with the pulse sequence shown in Fig. 1. These measurements served to check the operational capability of the 13-interval STEMSI pulse sequence for velocity mapping in natural porous media under the influence of internal magnetic field gradients. In each direction perpendicular (x- and y-directions) and parallel (z-direction) to the induced water flow direction, flow-encoded MR images were acquired. Since the flow was applied in the z-direction we expected that the average velocity under parallel flow encoding deviates from zero. However, the average velocity with perpendicular flow encoding should be zero with a non-vanishing standard deviation. These fluctuations around zero velocity result from the motion of water molecules around the sand grains (acting as barriers to the flow).

The velocity maps and 1D mean velocity profiles for a pore flow velocity of $v_{app,max} = 1.35$ mm/s are shown in Fig. 2. Note that for the 1D profiles the velocities in the y-direction have been averaged (as opposed to arbitrarily selecting one particular line in the center of the velocity map).

The left column of Fig. 2 shows the velocity map of flow encoding in the z-direction (top) and the corresponding 1D mean velocity profile with spatial resolution in the x-direction (bottom). The velocities in the sand column (Fig. 2, top left) are evenly distributed over the cross-section around a positive mean value. This becomes even more obvious in the 1D velocity profile (Fig. 2, bottom left). Although mean velocities are different for each x-position, they clearly take positive values. The right hand side of Fig. 2 shows the velocity map (top) and the 1D mean velocity profile (bottom) for flow encoding perpendicular to the induced water flow. In contrast to velocity mapping parallel to the induced water flow (Fig. 2, top left), no significant positive or negative trend for velocities is seen (Fig. 2 top right). Also, the 1D mean velocity profile (Fig. 2, bottom right) fluctuates both positively and negatively around zero, with an average of zero. This confirms our stated assumption of a net zero velocity regarding the direction perpendicular to the induced water flow.

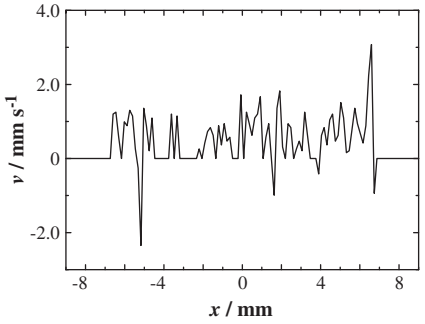

Fig. 3. 1D velocity profile along a single line as taken from the map in Fig. 2 (top left) for the highest applied pore velocity of $v_{app,max} = 1.35$ mm/s. Shown is the result of flow encoding parallel (z-direction) to the induced water flow. The observation time is 17 ms.

While the profiles in Fig. 2 are averaged values along the y-direction, Fig. 3 shows the profile of a single line taken in the center of the top left map as shown in Fig. 2. As expected, velocities are fluctuating much more and extracted numbers correspond now to the averaged velocity within one voxel. Note, however, that individual voxels may be partially or entirely occupied by a sand grain and zero velocity means in that case no velocity (nor signal) at all.

The maximum error of the averaged velocity in each voxel was estimated to ±40 μm/s. This is based on the range of velocities obtained for the lowest applied flow of $v_{app,0} = 20$ μ m/s. The method fails in this case and extracted local velocities may no longer be reliable. Therefore, we consider ±40 μm/s to be a safe upper limit for the uncertainties. However, the mean velocities in both profiles of Fig. 2 show significantly higher fluctuations. Especially in the range of $x = [-4; 4]$, where the average is done over a substantial number of pixels, the fluctuations around the mean value remain

significantly higher compared to the uncertainties and they seem to be the same both for parallel and perpendicular flow-encoding measurements. This would be in line with our expectation of water molecules moving around the sand grains. These observations for both parallel and perpendicular flow-encoding measurements prove the validity of the 13-interval STEMSI pulse sequence in natural porous media, even under the influence of internal magnetic field gradients.

In further experiments, the applied pore flow velocity was reduced in several steps down to the lowest value of $v_{app,0} = 0.02$ mm/s, where differences between the velocity maps for parallel and perpendicular flow encoding were no longer observable (data not shown). However, pore flow velocities have been reliably detected for velocities as low as $v_{app,min} = 0.06$ mm/s, although with the same absolute uncertainty of ±40 μm/s. The corresponding velocity maps and the 1D velocity profiles of these experiments are shown in Fig. 4.

When comparing Figs. 2 and 4 it becomes obvious that the flow field simply scales with the applied pore velocity. Apart from the absolute sizes (note the different scales used for the two figures), the 2D as well as the 1D velocity distributions are similar to each other. The same holds for the magnitude of the fluctuations with respect to the mean velocity values. It is this similarity between the velocity maps – only scaling with the mean velocity – which proves the reliability of the method even for mean pore flow velocities below 0.1 mm/s.

To further elucidate the obtained velocity distributions, we analyzed the NMR data by means of histograms, taking into account all pixels of the acquired velocity maps. This is shown in Fig. 5 for the highest applied pore flow velocity of $v_{app,max} = 1.35$ mm/s.

A Gaussian distribution of velocities with a mean of $v_{Gauss} = (0.81 \pm 0.01)$ mm/s and a standard deviation of $\sigma_{Gauss} = (0.94 \pm 0.02)$ mm/s fits well to the histogram of velocities shown in Fig. 5. The distribution of the experimental data is symmetric around its mean value. Due to a higher standard deviation of velocities compared to the mean velocity, negative velocities also appear in the histogram. This means that in some pixels water

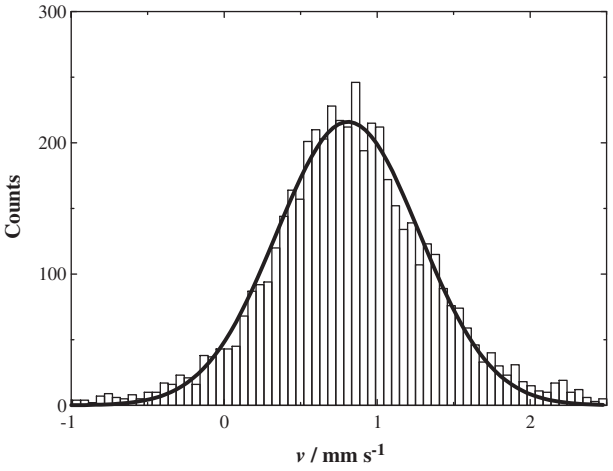

Fig. 5. Histogram of the NMR detected pore flow velocity distribution in the velocity map of the highest applied pore flow velocity of $v_{app,max} = 1.35$ mm/s (rectangles). A Gaussian function is fitted to the data (line).

is flowing in the opposite direction, an observation which is also evident from Fig. 3. The reason for this behavior is again the evasive movement of water molecules around grains of sand. Since the velocity maps reflect only the projection of the actual velocity vector of each pixel in the observed direction, velocities with negative values are possible.

In order to calibrate the mean pore flow velocities we obtain from NMR flow imaging in the sand column, we also acquired the velocity field of water flowing in a pipe under otherwise identical conditions. We obtained the characteristic parabolic profile as one would expect in a pipe. One example for a flow rate of $v_{mean} = 0.9$ mm/s is given in Fig. 6.

Similar velocity profiles have been measured for mean flow rates in the pipe from 3.5 mm/s down to 50 μm/s. The root mean square deviation of the measured local velocities from the fitted

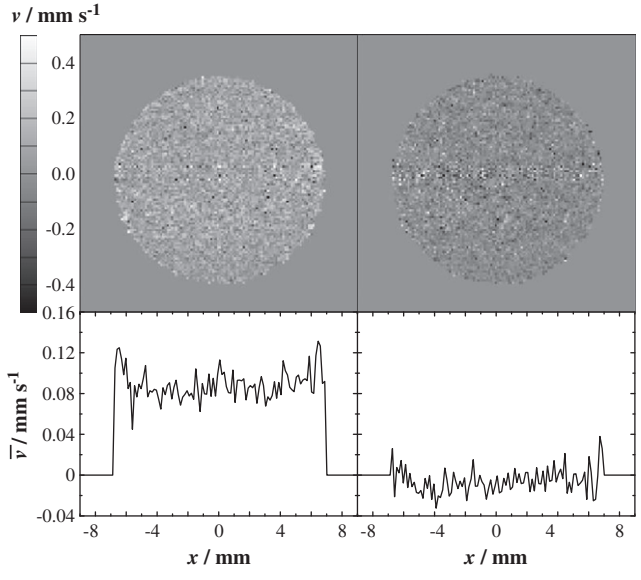

Fig. 4. Velocity maps (top) and 1D mean velocity profiles (bottom) of the lowest applied pore velocity of $v_{app,min} = 0.06$ mm/s, where flow was still detectable, using the pulse sequence 13-interval STEMSI. Shown are the results of flow encoding parallel (z-direction, left) and perpendicular (x-direction, right) to the induced water flow direction. The observation time is 17 ms. Note the different ranges in the velocity scales compared to Fig. 2.

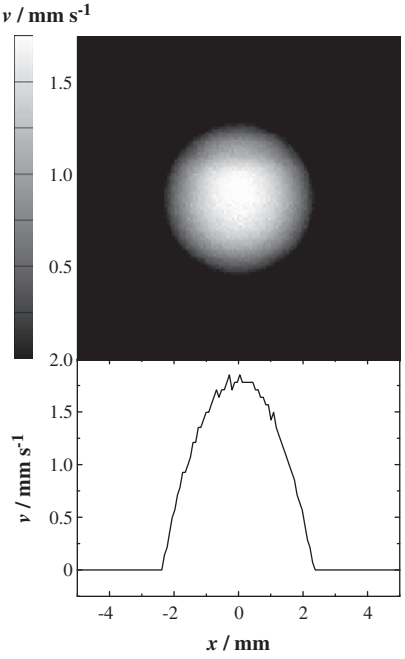

Fig. 6. Velocity map (top) and 1D velocity profile (bottom) of water flowing in a pipe with an applied mean velocity of $v_{mean} = 0.9$ mm/s. Note, the 1D profile in this figure is not an average along y but a slice across the center of the 2D profile.

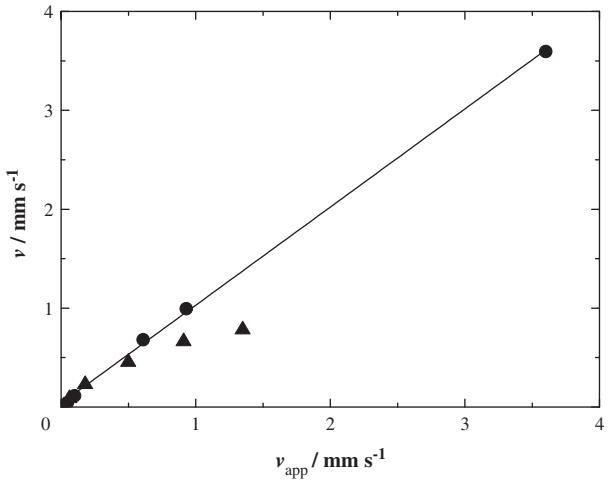

Fig. 7. Comparison of the applied pore flow velocity and the experimental determined mean pore flow velocity, averaged over the entire velocity map detected with the pulse sequence 13-interval STEMSI. Shown are measurements of the flow of water with 0.1 wt% $CuSO_4$ through a simple tube (dots) for calibration and through the sand column (triangles). The black line is a linear fit to the mean velocities of the calibration measurement through the tube.

parabolic profile is 7 μm/s for all velocities. We expect a linear relation between the mean velocity as measured by NMR and the applied flow velocity. Ideally, the factor between both velocities would be unity. The result of these measurements is plotted as the black dots in Fig. 7.

As seen from Fig. 7, the linear relationship between the NMR data and the applied velocities is very good in the case of pipe flow. The linear fit equation is $v = (1.01 \pm 0.01) \times v_{app}$ so that no correction factor between the measured and applied velocity is needed. This holds even for very high applied velocities. Note that the relationship is different to that where water flows through the sand column (black triangles). At low applied pore flow velocities, the experimentally detected mean pore flow velocity matches with the applied value within uncertainties. However, with higher applied pore flow velocities an increasing deviation from the expected value towards smaller velocities is observed. Based on the results we obtained from the pipe flow, which were obtained under identical conditions only with the sand column replaced by the pipe, we may exclude leakage or evaporation as a cause for the observed velocity discrepancy in the sand column. We may also exclude excessively high phase encoding gradients (which may result in phase aliasing) as the field of velocity was chosen large enough to accommodate even velocities larger by 10 times, compared to the applied mean pore flow velocity.

Although the main focus of this work was on the detection of small pore flow velocities (where no deviation was observed), we still set out to investigate the deviation at higher applied pore flow velocities. In a first step, we evaluated the magnitude maps as obtained from the modulus of the MR images without a phase-encoding gradient and their corresponding 1D intensity profiles as shown in Fig. 8. Note that for the 1D profiles the magnitudes in the y-direction have been averaged.

It is evident from Fig. 8 that the total NMR signal intensity decreases with increasing mean pore flow velocity. While the left hand side of Fig. 8 shows the intensity map for an applied pore flow velocity of $v = 0.06$ mm/s, the right hand side represents the intensities at $v = 1.35$ mm/s. As for the velocity maps, the profile of the intensity maps is similar for both velocities. However, the total intensity is only half the value for the higher velocity. A more quantitative analysis of this relationship between the NMR signal intensity and the applied pore flow velocity is shown in Fig. 9.

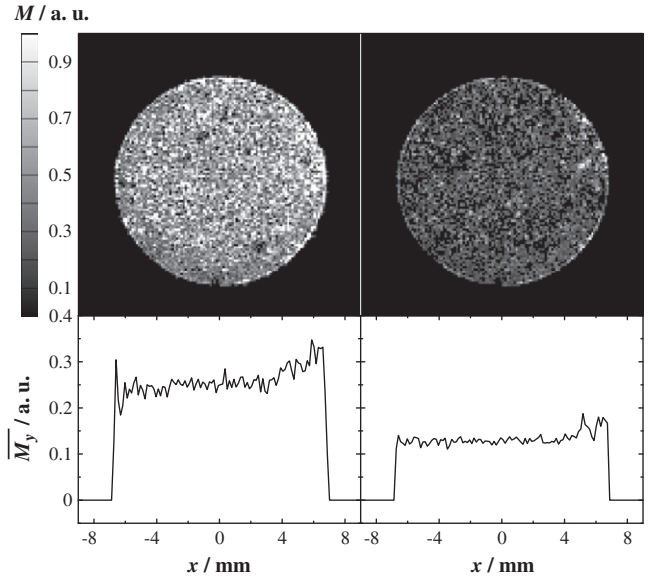

Fig. 8. NMR signal intensity maps (top) and 1D mean intensity profiles (bottom) of the lowest NMR detectable applied pore flow velocity of $v_{app,min} = 0.06$ mm/s (left), and the highest applied pore velocity $v_{app,max} = 1.35$ mm/s (right) using the pulse sequence 13-interval STEMSI. The observation time is 17 ms.

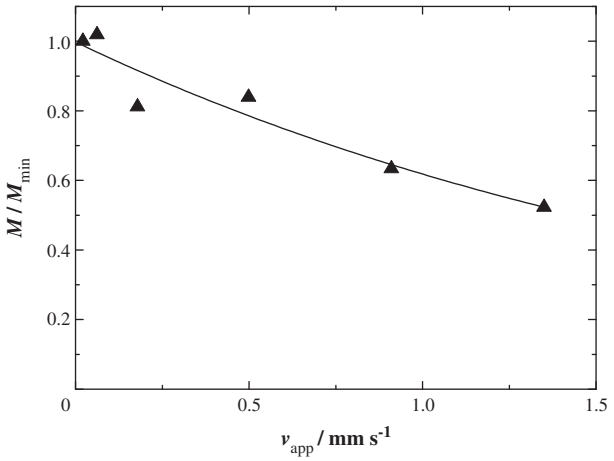

Fig. 9. Plot showing the dependence of signal magnitude integrated over the entire selected slice from the applied pore flow velocity (triangles). The magnitude is normalized by the integrated magnitude of the lowest applied pore flow velocity of $v_{app,0} = 0.02$ mm/s. The data are fitted with an exponential decay (line).

The data points shown as triangles in Fig. 9 were calculated by integrating the magnitude of the entire selected slice for each chosen pore flow velocity, followed by normalization by the integrated magnitude of the lowest applied pore flow velocity of $v_{app,0} = 0.02$ mm/s. A decay of the signal magnitude with increasing applied flow velocity is evident and may be fitted by an exponential decay (black line in Fig. 9). Thus, even with the 13-interval STEMSI, which reduces or even cancels influences of internal magnetic field gradients on the NMR signal, we still detect a magnitude loss with increasing applied pore flow velocity. Therefore, we now discuss possible reasons for the NMR signal decay in the light of Eq. (1), taking into account the influences of relaxation, diffusion/dispersion and flow. Furthermore, we relate this discussion to the observed deviations of the detected mean pore flow velocities from their expected value at high applied pore flow velocities.

T_2 relaxation has impact on the signal during the four time intervals τ shown in the pulse sequence, Fig. 1. During the storage

time, Δ', where the magnetization is stored along the z-direction, no T_2 relaxation occurs. Since τ was always kept at the same value, the influence of T_2 relaxation on the detected signal should stay the same, independent of the applied pore flow velocity. Furthermore, the overall influence of T_2 relaxation should be moderate. The T_2 distribution exhibits three peaks at 20 ms, 50 ms (similar in intensity) and a minor peak at 160 ms. Considering the rf-pulse distance, $\tau = 2.3$ ms, the reduction of the 20 ms peak is about 40%, 20% for the peak at 50 ms and negligible for the remaining one.

We may also exclude a change of the sample via repacking of the sand over the duration of the experiments since the T_1 relaxation time (0.23 s and 1.1 s with and without the $CuSO_4$, respectively) and the diffusion coefficient before and after flow experiments (data not shown) show no differences in the observed values.

Recently, Homan et al. [32] investigated flow in porous media (a column of randomly packed porous aluminum oxide beads, among others) and the influence of internal magnetic field gradients on measured flow-related parameters. Similar to our results they report an NMR signal decay being dependent on the observation time as well. It is important in this context that a comparable signal loss was not observed for the water flowing in the pipe.

More interestingly, Homan et al. [32] found a dependency of the velocity as measured with NMR on the observation time, to which they link the effects of surface relaxation, susceptibility and dispersion (for the latter one see also Kandhai et al. [42]). In order to explore this further, additional flow investigations had been undertaken. In these measurements the applied pore flow velocity was kept constant at the highest applied value of $v_{app,max} = 1.35$ mm/s, while the observation time was varied in the range from $\Delta_{min} = 9$ ms up to $\Delta_{max} = 50$ ms. In Fig. 10 we plot the mean value averaged over all velocities in one slice (for any given applied flow velocity) against the observation time, Δ. Note that τ was kept constant as well, ensuring a constant influence of T_2 relaxation. It is clear from Fig. 10 that the detected velocity decreases with increasing observation time, in line with the observations by Homan et al. [32].

This observed decrease of the detected velocities, dependent on the observation time, can be described empirically with an exponential decay (black line in Fig. 10) with a time constant of $T' = (33 \pm 3)$ ms. Assuming that the velocity at $\Delta = 0$ ms represents the actual mean pore flow velocity in the sample, the exponential function was extrapolated to $\Delta = 0$ ms. The resulting mean pore flow velocity is $v_{fit} = (1.2 \pm 0.1)$ mm/s. This matches reasonably well with the applied pore flow velocity of $v_{app,max} = 1.35$ mm/s.

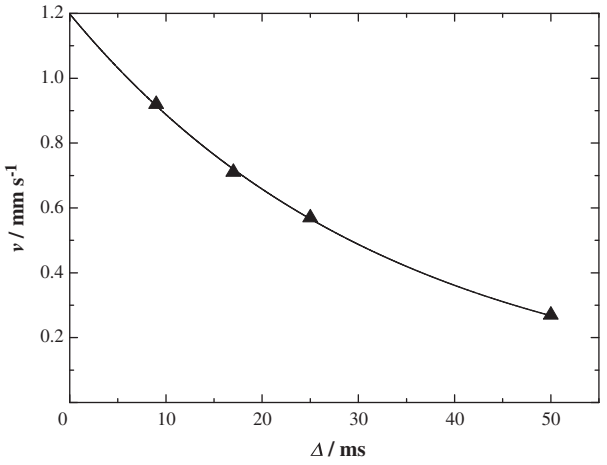

Fig. 10. Dependence of the velocity detected with flow encoding on the observation time Δ at the applied pore flow velocity of $v_{app,max} = 1.35$ mm/s with 13-interval STEMSI pulse sequence (triangles). An exponential decay is fitted to the data (line).

Although the extrapolated velocity is close to the expected value, a small discrepancy remains. This may be due to a residual influence of the internal gradients and the violation of their constancy during the observation time, in particular at higher velocities. However, this artifact does not appear at low applied pore flow velocities, which was the main focus of this work.

Besides the already discussed effects (which are related to the nature of the sample as a porous material and the fluid flow in it) we may further consider artifacts linked to the merging of the imaging subsequence into the 13-interval pulse sequence (see Fig. 1). In particular the slice selective (third) $\pi/2$ pulse may be the source of experimental errors. To investigate this further we altered the pulse sequence and swapped the slice selective pulse with the first rf-pulse. This results in slice selective excitation and a hard $\pi/2$ pulse after the storage time, Δ'. Despite this alteration we obtained identical results for extracted velocities as well as NMR signal intensities. Second, we compared signal intensities as well as velocities for the different slices taken in the case of pipe flow (see Fig. 6). We found no noticeable differences between slices, in particular there were no differences if one compares slices sandwiched between other slices and those on the top or bottom of the 3D image. Third, we reduced the resolution in the phase direction (using only eight phase steps). Obviously, this leads to a velocity average over several pores: nonetheless, the obtained total flux (as an integral over the entire slice) was conserved.

To conclude, we found the 13-interval STEMSI to be robust and tend to attribute the observed deviations at higher velocities to artifacts arising from heterogeneity of the sample rather than from the pulse sequence employed. More work would be necessary to fully understand these deviations. However, for the velocities of interest (those below 0.1 mm/s), we showed in this work that NMR using the 13-interval STEMSI pulse sequence is a powerful technique for investigating flow in natural porous media which strongly influence the NMR signal by internal magnetic field gradients.

5. Conclusion

In this work we investigated flow in a model soil system consisting of natural sand. Mean velocities as small as 60 μm/s have been successfully monitored for the first time, to our knowledge. The 13-interval STEMSI pulse sequence seems therefore to be suitable for investigating water motion in soil due to root water uptake and may provide a basis for deeper understanding of the mechanisms linked to this process. Accompanying measurements of laminar pipe flow yield detectable velocity differences below 10 μm/s at mean velocities of 50 μm/s. This is similar to recent achievements by van de Meent et al. [21] and confirms that such small velocities can be reliably detected by NMR.

Deviations of the measured velocities at higher flow rates were found to depend on the observation time and appear to be linked to an additional loss of magnetization at higher flow rates.

The 13-interval STEMSI pulse sequence proves to be a powerful tool with which to investigate slow flow processes in natural porous media. Its strength (and advantage compared to conventional stimulated echo methods) lies in the reduced or even canceled impact of internal magnetic field gradients on both the magnitude of the NMR signal as well as the imparted phase shift due to the phase encoding gradients.

Acknowledgments

We gratefully acknowledge financial support by German Academic Exchange Service (DAAD), the Virtual Institute of Portable

NMR funded by the Helmholtz Association (HGF) as well as the New Zealand Foundation for Research Science and Technology.

References

[1] Y. Waisel, A. Eshel, U. Kafkafi, Plant Roots: The Hidden Half, Marcel Dekker Inc., New York, 1991.
[2] P.J. Gregory, Plant Roots: Growth, Activity and Interactions with Soils, Blackwell, Oxford, 2006.
[3] M. Javaux, M. Vanclooster, Scale- and rate-dependent solute transport within an unsaturated sandy aquifer, Soil Sci. Soc. Am. J. 67 (2003) 1334–1343.
[4] L. Weihermüller, J. Siemens, M. Deurer, S. Knoblauch, H. Rupp, A. Göttlein, T. Pütz, In-situ soil water extraction: a review, J. Environ. Qual. 36 (2007) 1735–1748.
[5] W. Köckenberger, C. De Panfilis, D. Santoro, P. Dahiya, S. Rawsthorne, High resolution NMR microscopy of plants and fungi, J. Microsc. (Oxford) 216 (2) (2004) 182–189.
[6] M.I. Menzel, A.M. Oros-Peusquens, A. Pohlmeier, N.J. Shah, U. Schurr, H.U. Schneider, Comparing ^{1}H-NMR imaging and relaxation mapping of German white asparagus from five different cultivation sites, J. Plant Nutr. Soil Sci. 170 (2007) 24–38.
[7] J.M. Brown, P.J. Kramer, G.P. Cofer, G.A. Johnson, Use of nuclear magnetic resonance microscopy for noninvasive observations of root–soil water relations, Theor. Appl. Climatol. 42 (1990) 229–236.
[8] M.W. Jennette, T.W. Rufty, J.S. MacFall, Magnetic resonance image visualization of plant roots in situ: a tool for characterizing root morphology, in: Digital Imaging and Spectral Techniques: Applications to Precision Agriculture and Crop physiology, vol. 66, Madison, 2003, pp. 65–72.
[9] N. Nestle, T. Baumann, R. Niessner, Magnetic resonance imaging in environmental science, Environ. Sci. Technol. 36 (7) (2002) 154 A–160 A.
[10] A. Pohlmeier, A.M. Oros-Peusquens, M. Javaux, M.I. Menzel, H. Vereecken, N.J. Shah, Investigation of water content and dynamics of a ricinus root system in unsaturated sand by means of SPRITE and CISS: correlation of root architecture and water content change, Magn. Reson. Imaging 25 (2007) 579–580.
[11] A. Pohlmeier, A.M. Oros-Peusquens, M. Javaux, M.I. Menzel, J. Vanderborght, J. Kaffanke, S. Romanzetti, J. Lindenmair, H. Vereecken, N.J. Shah, Changes in soil water content resulting from ricinus root uptake monitored by magnetic resonance imaging, Vadose Zone J. 7 (3) (2008) 1010–1017.
[12] E. Garrigues, C. Doussan, A. Pierret, Water uptake by plant roots: I – Formation and propagation of a water extraction front in mature root systems as evidenced by 2D light transmission imaging, Plant Soil 283 (2006) 83–98.
[13] C. Doussan, A. Pierret, E. Garrigues, L. Pagés, Water uptake by plant roots: II – Modelling of water transfer in the soil root-system with explicit account of flow within the root system-comparison with experiments, Plant Soil 283 (2006) 99–117.
[14] M. Javaux, T. Schröder, J. Vanderborght, H. Vereecken, Use of a three-dimensional detailed modeling approach for predicting root water uptake, Vadose Zone J. 7 (3) (2008) 1079–1088.
[15] P.T. Callaghan, Principles of Nuclear Magnetic Resonance Microscopy, Clarendon Press, Oxford, 1991.
[16] S.-I. Han, O. Marseille, C. Gehlen, B. Blümich, Rheology of blood by NMR, J. Magn. Reson. 152 (2001) 87–94.
[17] P. Galvosas, P.T. Callaghan, Fast magnetic resonance imaging and velocimetry for liquids under high flow rates, J. Magn. Reson. 181 (1) (2006) 119–125.
[18] T.W.J. Scheenen, D. van Dusschoten, P.A. de Jager, H. van As, Microscopic displacement imaging with pulsed field gradient turbo spin-echo NMR, J. Magn. Reson. 142 (2000) 207–215.
[19] T.W.J. Scheenen, F.J. Vergeldt, C.W. Windt, P.A. de Jager, H. van As, Microscopic imaging of slow flow and diffusion: a pulsed field gradient stimulated echo sequence combined with turbo spin echo imaging, J. Magn. Reson. 151 (2001) 94–100.
[20] C.F. Jenner, Y. Xia, C.D. Eccles, P.T. Callaghan, Circulation of water within wheat grain revealed by nuclear magnetic resonance micro-imaging, Nature 336 (1988) 399–402.
[21] J.-W. van de Meent, A.J. Sederman, L.F. Gladden, R.E. Goldstein, Measurement of cytoplasmatic streaming in single plant cells by magnetic resonance velocimetry, J. Fluid Mech. 642 (2010) 5–14.
[22] T. Schulze-Till, I. Kaufmann, B. Sattelmacher, P. Jakob, A. Haase, S. Guo, U. Zimmermann, L. Wegner, A ^{1}H NMR study of water flow in *Phaseolus vulgaris* L. roots treated with nitrate or ammonium, Plant Soil 319 (2009) 307–321.
[23] A. Pohlmeier, D. van Dusschoten, L. Weihermüller, U. Schurr, H. Vereecken, Imaging water fluxes in porous media by magnetic resonance imaging using D_20 as a tracer, Magn. Reson. Imaging 27 (2009) 285–292.
[24] M. Rokitta, U. Zimmermann, A. Haase, Fast NMR flow measurements in plants using FLASH imaging, J. Magn. Reson. 137 (1999) 29–32.
[25] P. Mansfield, P.G. Morris, NMR imaging in biomedicine, Adv. Magn. Reson. (Suppl.2) (1982) 1–343.
[26] N.M. Homan, C.W. Windt, F.J. Vergeldt, E. Gerkema, H. Van As, 0.7 and 3 T MRI and sap flow in intact trees: xylem and phloem in action, Appl. Magn. Reson. 32 (2007) 157–170.
[27] D. Guilfoyle, P. Mansfield, K. Packer, Fluid flow measurements in porous media by echo-planar imaging, J. Magn. Reson. 97 (1992) 342–358.
[28] R.A. Waggoner, E. Fukushima, Velocity distribution of slow fluid flows in Bentheimer sandstone: an NMRI and propagator study, Magn. Reson. Imaging 14 (1996) 1085–1092.
[29] C. Chang, A. Watson, NMR imaging of flow velocity in porous media, AIChE 45 (1999) 437–440.
[30] L.D. Anadon, H.M. Lim, A.J. Sederman, L.F. Gladden, Hydrodynamics in two-phase flow within porous media, Magn. Reson. Imaging 23 (2005) 291–294.
[31] L. Li, Q. Chen, A.E. Marble, L. Romero-Zerón, B. Newling, B.J. Balcom, Flow imaging of fluids in porous media by magnetization prepared centric-scan SPRITE, J. Magn. Reson. 197 (2009) 1–8.
[32] N.M. Homan, B. Venne, H. Van As, Flow characteristics and exchange in complex biological systems as observed by pulsed-field-gradient magnetic-resonance imaging, Phys. Rev. E 82 (2010) 026310.
[33] R.M. Cotts, M.J.R. Hoch, T. Sun, J.T. Markert, Pulsed field gradient stimulated echo methods for improved NMR diffusion measurements in heterogeneous systems, J. Magn. Reson. 83 (2) (1989) 252–266.
[34] A.J. Lucas, S.J. Gibbs, E.W.G. Jones, M. Peyron, J.A. Derbyshire, L.D. Hall, Diffusion imaging in the presence of static magnetic-field gradients, J. Magn. Reson. A 104 (1993) 273–282.
[35] K.V. Romanenko, B.J. Balcom, Permeability mapping in porous media by magnetization prepared centric-scan SPRITE, Exp. Fluids 50 (2011) 301–312.
[36] R.F. Karlicek, I.J. Lowe, A modified pulsed gradient technique for measuring diffusion in the presence of large background gradients, J. Magn. Reson. 37 (1980) 75–91.
[37] P. Galvosas, F. Stallmach, J. Kärger, Background gradient suppression in stimulated echo NMR diffusion studies using magic pulsed field gradient ratios, J. Magn. Reson. 166 (2) (2004) 164–173.
[38] J.E. Tanner, Use of the stimulated echo in NMR diffusion studies, J. Chem. Phys. 52 (1970) 2523.
[39] S.L. Codd, S.A. Altobelli, A PGSE study of propane gas flow through model porous bead packs, J. Magn. Reson. 163 (1) (2003) 16–22.
[40] F. Stallmach, P. Galvosas, Spin echo NMR diffusion studies, Annu. Rep. NMR Spectrosc., vol. 61, Elsevier, Amsterdam, Boston, Heidelberg, 2007, pp. 51–131.
[41] N. Spindler, A. Pohlmeier, P. Galvosas, Water flow investigation on quartz sand with 13-interval stimulated echo multi-slice imaging, AIP Conf. Proc. 1330 (1) (2011) 73–76.
[42] D. Kandhai, D. Hlushkou, A.G. Hoekstra, P.M.A. Sloot, H. Van As, U. Tallarek, Influence of stagnant zones on transient and asymptotic dispersion in macroscopically homogeneous porous media, Phys. Rev. Lett. 88 (23) (2002) 234501.